Experimental Mechanics (2006) 46: 805–824
DOI 10.1007/s11340-006-0296-7

A Novel Fluid Structure Interaction Experiment to Investigate Deformation of Structural Elements Subjected to Impulsive Loading

H.D. Espinosa · S. Lee · N. Moldovan

Received: 20 June 2006 / Accepted: 31 August 2006 / Published online: 8 December 2006

Abstract This paper presents a novel experimental methodology for the study of dynamic deformation of structures under underwater impulsive loading. The experimental setup simulates fluid–structure interactions (FSI) encountered in various applications of interest. To generate impulsive loading similar to blast, a specially designed flyer plate impact experiment was designed and implemented. The design is based on scaling analysis to achieve a laboratory scale apparatus that can capture essential features in the deformation and failure of large scale naval structures. In the FSI setup, a water chamber made of a steel tube is incorporated into a gas gun apparatus. A scaled structure is fixed at one end of the steel tube and a water piston seals the other end. A flyer plate impacts the water piston and produces an exponentially decaying pressure history in lieu of explosive detonation. The pressure induced by the flyer plate propagates and imposes an impulse to the structure (panel specimen), which response elicits bubble formation and water cavitations. Calibration experiments and numerical simulations proved the experimental setup to be functional. A 304 stainless steel monolithic plate was tested and analyzed to assess its dynamic deformation behavior under impulsive loading. The experimental diagnostic included measurements of flyer impact velocity, pressure wave history in the water, and full deformation fields by means of shadow moiré and high speed photography.

H.D. Espinosa (✉, SEM member) · S. Lee · N. Moldovan
Department of Mechanical Engineering,
Northwestern University, 2145 Sheridan Rd.,
Evanston, IL 60208-3111, USA
e-mail: espinosa@northwestern.edu

Keywords Fluid–structure interaction · Underwater impulsive loading · Dynamic structural deformation

Introduction

Development of blast-resistant materials and structures is a critical engineering problem in various applications, including plants which need provision against emergency explosion such as in oil, chemistry or nuclear industries, and obviously military or civil transportation vehicles in which the possibility of impulsive loading is always present. In this regard, sandwich structures having core materials between two face sheets have been extensively investigated as a means to increase strength and stiffness or reduce weight. Xue and Hutchinson [21, 22] and Hutchinson and Xue [6] performed detailed computational simulations to assess the performance of metal sandwich plates subjected to impulsive blast loads. To gain insight into the efficiency of steel sandwich structures, these authors modeled the underwater structure by imposing an initial momentum to the face sheet in contact with the fluid, under the assumption that the blast pulse period is sufficiently short. Also, they determined the momentum impulse which needs to be applied to the face sheet based on Taylor's work [18] neglecting the resistance offered by the core-bottom face sheet to the top face sheet. This preliminary work demonstrated that sandwich structures with various core topologies (honeycomb, folded beam, pyramidal truss) offer an advantage over solid plates, of equal mass per unit area, in the sense that they can absorb a much larger impulse for a given maximum central displacement. Qui et al. [10–12], Fleck and

Deshpande [4], and Deshpande and Fleck [2] also investigated sandwich panels with cellular cores. These authors formulated an analytical model to describe the overall deformation and strength of sandwich panels subjected to impulse loading. Their model suggested that the response of such structures can be separated into three main stages: Stage I: impulse loading of front sheet; Stage II: core compression phase and load transferring to back sheet; and Stage III: plate deflection and stretching (overall structural response). The existence and limitation of this multistage deformation process was later analyzed in [9]. In this later work the relevance of the front sheet and core stiffness in the context of fluid-structure interactions was assessed. Through extensive numerical simulations, they showed that thin front sheets and low density cores perform better.

As an alternative to the development of sandwich structures, researchers have pursued the design of metal alloys in which very high strength is achieved while reasonable levels of ductility are preserved. For instance, Vaynman et al. [19, 20] developed high performance hot-rolled and air-cooled low-carbon steels, called NUCu steels, that show improvement in toughness, strength, weldability and weatherability. These material have low carbon content and the satrengthening is mainly derived from copper-precipitation on air-cooling from hot rolling; nickel, niobium, and titanium are added to improve the manufacturing process and control the grain size. For example, NUCu-100 steel can reach yield strength of 712 MPa, tensile strength of 780 MPa and elongation at break of 26.3%; this material shows also very high Charpy impact energies at cryogenic temperatures [20]. Hao et al. [5] developed a multi-scale hierarchical constitutive model for the computational design of metal alloys. The approach was used to relate quantum mechanical, micromechanical, and overall strength/toughness properties. This model, which can account for different kinds of alloy matrix inclusions, was implemented in a FEM code for the design of ultrahigh strength, high toughness steels. The aforementioned material multiscale model is particularly suitable to the development of blast resistant alloys.

The above theoretical, computational and experimental work points at the need for developing fluid–structure interaction (FSI) experiments without major aprioristic assumptions, which can elucidate the mechanisms of deformation and fracture of blast resistant structures and materials. The experimental setup should generate blast loadings in water and have dimensions representative of underwater explosion full field problems. In doing so, we expect to measure structural rather than solely constitutive material response under a realistic, although scaled, fluid–structure interaction event.

In this paper the underwater explosion impinging on a naval hull structure problem is defined and an experimental setup to reproduce it is proposed. Then we analyze the fundamental design steps that have leaded to the development of the FSI apparatus, with particular emphasis on its scaling. In addition, the experimental procedure is described and details on the diagnostic tools implemented to monitor projective velocity, pressure history, and specimen panel out-of-plane full field displacements are given. Two calibration experiments are then presented, and the experimental data is compared with a finite element model. The time-dependent behavior of the specimen and of the fluid is analyzed, with the finite element model, focusing on the cavitation that takes place at their interface.

Experimental Configuration

Problem Definition

Consider the pressure wave generated by an underwater explosion impinging on a naval hull structure, Fig. 1. Typically, a hull structural panel is clamped at the boundary and has a thickness of approximately 25.4 mm and a span width of 2 m. The free-field incident blast pulse in a fluid can be idealized as an exponential pressure decay, $p = p_0 e^{-t/t_0}$, where p_0 is the initial peak pressure and t_0 is a characteristic decay time [16]. The free-field momentum (impulse/area) is given by $I_0 = \int_0^\infty p\, dt = p_0 t_0$. For a typical blast $t_0 \sim 10^{-4}$ s, $p_0 \sim 100$ MPa, and $I_0 \sim 10^4$ N s/m^2, which correspond to the case of detonating 1 kg of TNT at 1 m distance from the structure or 1,000 kg of TNT at 10 m away in water [16, 17].

Fundamental Design

The proposed FSI experimental setup is depicted in Fig. 2. To generate an impulsive load, similar to that of an explosive blast, a flyer plate of thickness h_s is launched against water confined in a pressure tube or anvil. For a review of plate impact testing, see [3]. Assuming one dimensional elastic wave propagation and a linear equation of state for the fluid, one can achieve the pressure profile as a piece-wise function, namely,

$$P_N = \frac{sf}{s+f} V_0 \left[\frac{s-f}{s+f}\right]^N, N = 0, 1, \ldots\ldots, n \quad (1)$$

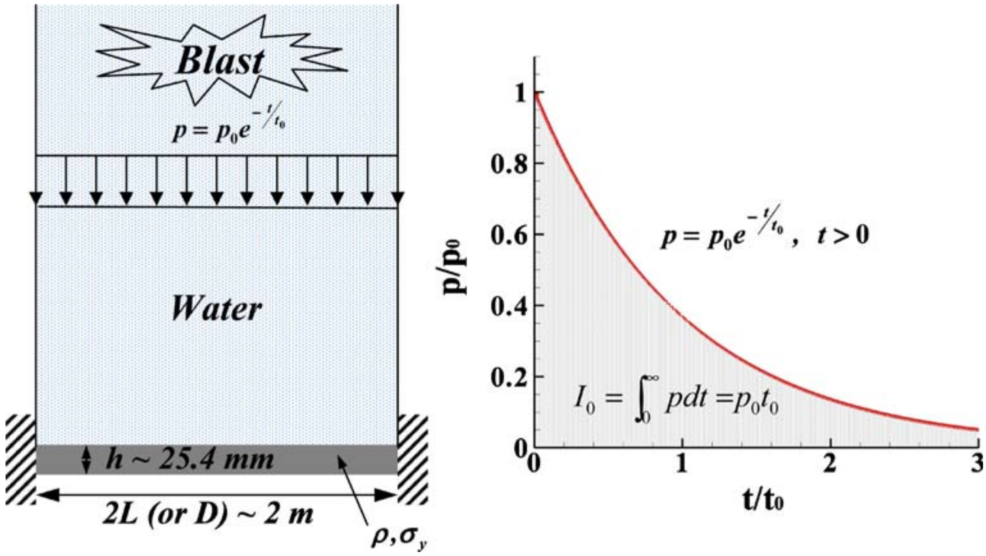

Fig. 1 Underwater blast loading onto a naval hull structure. Geometrical considerations (*left*), and pressure history (*right*)

where $f=(\rho c)_f$ and $s=(\rho c)_s$ are the acoustic impedances of the fluid and solid, respectively. V_0 is the impact velocity and N is the number of reverberations of the wave in the flyer. The time elapsed in each reverberation is $t_N = (2h_s/c_s)N$. This pressure history can be made equal to $p = p_0 e^{-t/t_0}$ from which the impact velocity can be related to the peak pressure and the flyer plate thickness to t_0:

$$V_0 = \frac{s+f}{sf} p_0 \tag{2}$$

and

$$e^{-t_N/t_0} = \left[\frac{s-f}{s+f}\right]^N, (2h_s/c_s) = -\frac{1}{t_0} \ln\left[\frac{s-f}{s+f}\right]. \tag{3}$$

By selecting the fluid and the material for the flyer plate, one can determine the thickness of the flyer plate such that exponential pressure decay with characteristic time t_0 is achieved. For example, the

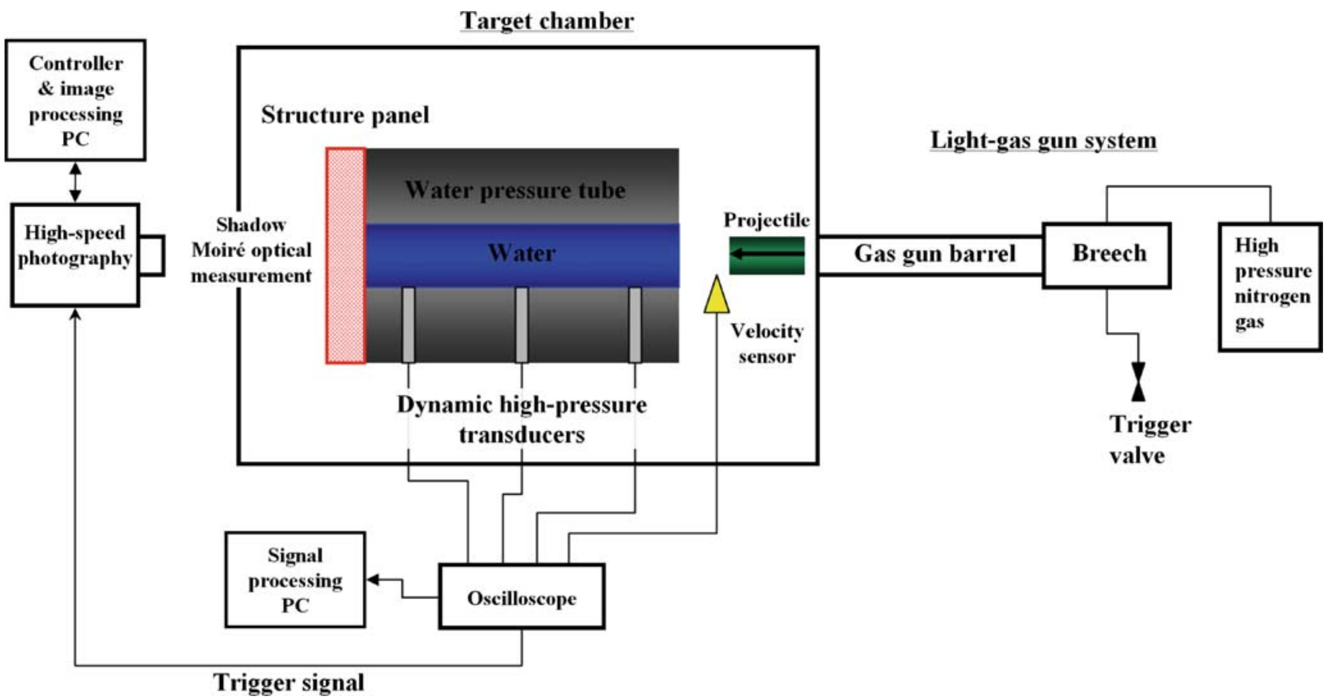

Fig. 2 Fluid–structure interaction (*FSI*) experimental configuration

pressure profile generated by the impact of an Al flyer plate, 5.3 mm-thick, against water is shown in Fig. 3. Selection of the initial pressure p_0 determines the initial impact velocity V_0 according to equation (2).

The above simple analysis shows that a flyer plate launched by a gas gun against water contained in an anvil can be employed to generate an exponentially decaying pressure history in lieu of explosive loading. The FSI experimental setup is instrumented with several sensors to measure the pressure history and other variables of interest, Fig. 2. The impact velocity of the flyer plate is measured by a contact-pin type velocity sensor [3]. The pressure history in the water is recorded by dynamic high pressure transducers and a digital oscilloscope while the deflection history of the specimen panel is measured optically by shadow moiré using a Cordin Intensified CCD Camera 220-8 high-speed camera.

Scaling Issues

There are other design parameters to be determined for simulating the full scale phenomena with the above laboratory FSI setup: sample panel radius R, sample panel thickness h, sample panel material properties such as density, ρ, yield stress, σ_y, and length of the anvil L_a. Note that the gas gun system utilized in this investigation has the following dimensional limitations: (a) the inside diameter of the gas gun barrel is 3" (76.2 mm), which limits the size of the impacting flyer plate and the inside diameter of the anvil at the impact end; and (b) the inside dimension of the target chamber (approximately 900 mm in length) which limits the length of the pressure tube. In full scale applications, panels of 2 m in width and 2.54 cm in thickness are

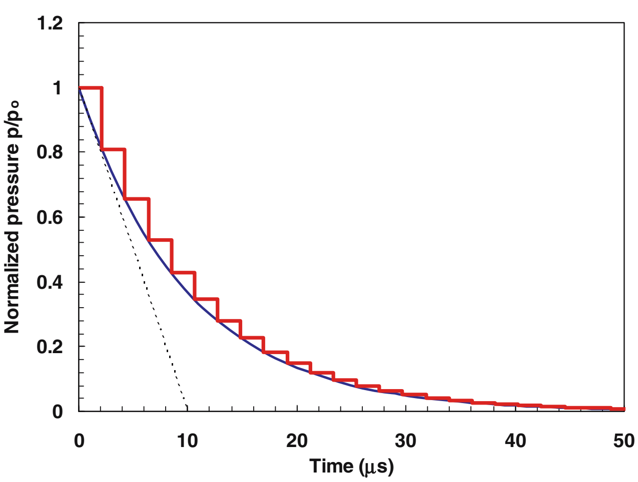

Fig. 3 Pressure profile at the water surface imposed by the impact of a 5.3 mm-thick Al flyer plate

typically employed. Hence, scaling down is essential in the development of FSI experiments.

For simplicity, in the scaling analysis a solid plate is considered as a sample panel. The optimization criterion is based on the maximum deflection of the system normalized by the span of the structure. However, the analysis is valid also for sandwich beams of various cores and other type of structures. Following the non-dimensional study by Xue and Hutchinson [21, 22], key dimensionless parameters relevant to the problem are: $\overline{M}/\rho R, t/\left(R\sqrt{\rho/\sigma_y}\right), I/\left(\overline{M}\sqrt{\sigma_y/\rho}\right)$, which define dimensionless mass per unit area, dimensionless time and dimensionless impulse, respectively. If we keep these parameters the same between full scale application and the laboratory experimental setup, we have:

$$\overline{M} = \rho h, \overline{M}/\rho R = h/R \tag{4}$$

$$\left(\frac{t}{R\sqrt{\rho/\sigma_y}}\right)_E = \left(\frac{t}{R\sqrt{\rho/\sigma_y}}\right)_F \tag{5}$$

$$\left(\frac{I}{\overline{M}\sqrt{\sigma_y/\rho}}\right)_E = \left(\frac{I}{\overline{M}\sqrt{\sigma_y/\rho}}\right)_F \tag{6}$$

where the subscript E denotes "experiment" and F "full scale." If the material employed in the experiments is the same as the one employed in the full scale application, the above conditions reduce to:

$$\left(\frac{h}{R}\right)_E = \left(\frac{h}{R}\right)_F, h_E = \frac{1}{K}h_F; \left(\frac{t}{R}\right)_E = \left(\frac{t}{R}\right)_F,$$
$$t_E = \frac{l}{K}t_F; \left(\frac{I}{h}\right)_E = \left(\frac{I}{h}\right)_F, I_E = \frac{1}{K}I_F,$$

where $K=R_F/R_E$ is the ratio of full scale and experimental panel radii (half span). Hence, for a full field dimension, the scaling factor K is determined by the panel size employed in the laboratory experiments. If the diameter of the specimen is selected as 76.2 mm, which is the maximum possible size of the flyer plate (limited by the diameter of the gun barrel), the scaling ratio would be 2,000/76.2=26.2. Therefore, a 25.4 mm thick solid plate is scaled down to 25.4 mm/26.2=0.97 mm, which is quite thin for accurate manufacturing and testing. Note that a sandwich panel specimen with the same mass per unit area would have face sheets thinner than 0.32 mm, which is very difficult to manufacture and test.

To obtain a more suitable scaling factor, the scaling of the plate diameter D (or $2R$) should overcome the dimensional limitation imposed by the flyer plate size. A diffuser-type pressure tube allows the implementa-

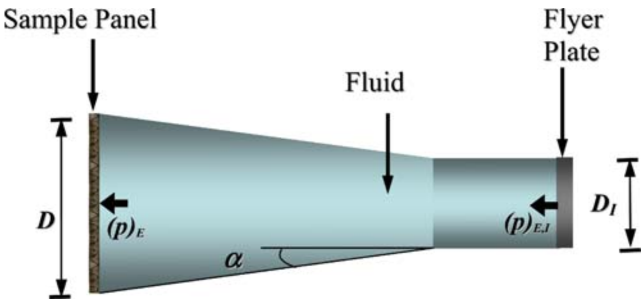

Fig. 4 Schematic of water chamber with divergent diffuser

tion of a larger sample diameter D as shown in Fig. 4. The diameter of the pressure tube entrance at the impact interface, D_I, should be smaller than the gas gun barrel diameter (76.2 mm in our laboratory gas gun). Utilizing this diffuser design, we could achieve a scaling factor of about 10. Hence, $h_E = 0.1h_F$, $t_E = 0.1t_F$, and $I_E = 0.1I_F$. Given D_I and D, the divergence of the tube characterized by the angle α was determined. The effect of α on the pressure profile was investigated by FE simulations and will be discussed later.

Another design objective is to obtain the same fluid-structure interaction as the one expected in the full scale application. In other words, the same fraction of the far field momentum, I_0, should be transmitted to the specimen. According to Taylor's analysis [18], the impulse impinging on the plate is given by

$$\frac{I}{I_0} = 2q^{q/(1-q)} \tag{7}$$

where the far field impulse is $I_0 = \int_0^\infty p dt = \int_0^\infty p_0 e^{-t/t_0} dt = p_0 t_0$ and $q = t_0/t^*$. The characteristic time scale t_* is given by

$$t^* = \frac{\rho h}{\rho_f c_f} \tag{8}$$

where ρ_f is the density of the fluid and c_f the sound speed of the fluid. To have the same momentum transfer, i.e., $(I/I_0)_E = (I/I_0)_F$, one needs to have the same q, namely,

$$\left(\frac{t_0 \rho_f c_f}{\rho h}\right)_E = \left(\frac{t_0 \rho_f c_f}{\rho h}\right)_F. \tag{9}$$

If the fluid and solid materials are the same in the full scale application and laboratory, this relation simplified as,

$$\left(\frac{t_0}{h}\right)_E = \left(\frac{t_0}{h}\right)_F, (t_0)_E = \frac{1}{K}(t_0)_F. \tag{10}$$

Hence the characteristic times also scale with factor K. As stated in the problem definition, for typical underwater explosions, $(t_0)_E$ is of the order of 100 μs, therefore, $(t_0)_F$ in the FSI experiments scales down to 10 μs, which is easily obtained with the appropriate flyer thickness according to equation (3).

The pressure p_0 does not scale down because it is an intensity quantity. This can be seen by substituting equation (10) into equation (6) as

$$I_E = \frac{1}{K} I_F, (p_0 t_0)_E = \frac{1}{K}(p_0 t_0)_F, (p_0)_E = (p_0)_F. \tag{11}$$

Because of the diffuser-type design of the pressure tube, the fluid pressure just ahead of the specimen panel, $(P_0)_E$, is lower than that next to the impact interface, $(P_0)_{E,I}$. Therefore, using momentum conservation one can determine the impact velocity needed to achieve a pressure p_0, viz.,

$$V_0 = \frac{s+f}{sf} \frac{D^2}{D_I^2} (p_0)_E. \tag{12}$$

Assuming the material of the flyer plate is steel, D_I~75 mm, D~200 mm, the above equation yields an impact velocity V_0 of the order of 300 m/s to achieve a peak pressure $(p_0)_E$~100 MPa. This is achievable in most gas gun facilities and, at the same time, it is in the range for which anvil and specimen recovery is possible permitting the post-mortem analysis of the specimens. We conducted extensive FEM simulations to gain further insight on the effect of the divergent diffuser and the nonlinearity in the response of water at the imposed pressures. The results confirmed the above analysis (see "Experimental Results" for a discussion of the simulation results).

Finally, the length of the pressure tube or anvil L_a should be selected so as to prevent the reflected pressure wave from interfering with the deflection of the sample plate. Xue and Hutchinson [22] reported that the response time for a steel plate of the type considered here with a span on the order of a meter or more is measured in several milliseconds. They also showed that the plate has a constant plastic energy, after dissipating the initial kinetic energy given by the impulse from the water, at $t\Big/\left(R\sqrt{\rho/\sigma_y}\right) = 1$. According to one dimensional wave propagation theory, the initial peak pressure will arrive at the sample plate at a time L_a/c_f after the flyer impact, and the reflected wave from the specimen will reach again the sample plate at a time $2L_a/c_f$ after the specimen initial loading. Therefore, the specimen plate response should be fully characterized during this period, i.e., $2L_a/c_f > \left(R\sqrt{\rho/\sigma_y}\right) =$ 0.6324 milliseconds, which translates into a pressure tube length L_a>0.468 m.

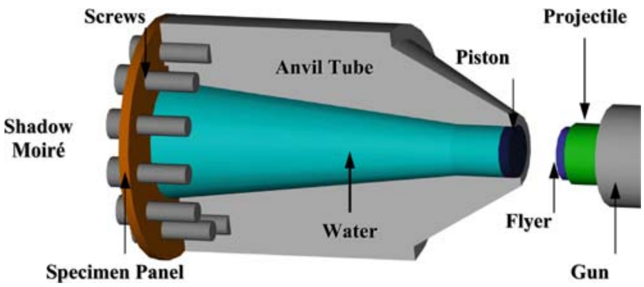

Fig. 5 Schematic of FSI test setup

Final Design and Setup

Based on the above scaling analysis, detailed FEM simulations (ABAQUS/Explicit 6.4-1) accounting for various wave phenomena in the fluid and structure were pursued. We examined the pressure wave propagation in the water and its distribution and history at the fluid–sample interface. Also, we evaluated the effects of reflection from different boundaries, pressure wave attenuation in the fluid, choice of diffuser angle, compressibility and cavitation of the water.

Figure 5 shows the schematic of the final design of the FSI test setup. Note that a 4140 steel piston was employed to seal the water at the entrance of the water pressure anvil tube. The design attempts to minimize the diffuser angle as we observed that large diffuser angles resulted in more spreading and partial loss of wavefront planarity. The entrance length (76.2 mm) of the uniform diameter was determined by the maximum travel distance of the piston and flyer plate. The diffuser angle of the final design was set to 7° as shown in Fig. 6. The dimensions of the water pressure anvil tube made of 4340 steel are given in Fig. 6. The diameter of the specimen exposed to the water blast pressure was chosen to be D=152.4 mm. To obtain a clamped boundary condition, 12 screws and a clamping ring were placed around the periphery of the specimen as shown in Figs. 6 and 7. The diameter of the screws was chosen to be 25.4 mm to sustain the blast loading. The outside diameter of the water pressure tube and the specimen panels were 292.1 mm to provide a space for the screws and their support. Figure 8 shows a projectile assembly consisting of a 4140 steel flyer plate, a PMMA flyer holder, a g-10 fiber glass tube, and an Al 6061 back piston. The set of parts excluding the flyer plate is typically referred to as sabot. The fiber glass tube and the Al back piston are common projectile components used in gas guns to launch the projectile. The PMMA flyer holder was machined with a tubular shape to connect the flyer plate to the fiber glass tube. Its mechanical impedance was made negligible in comparison with that of the flyer plate to properly simulate the exponentially decaying pressure wave as discussed in "Fundamental Design." To stop the sabot and avoid impact damage in the front face of the pressure tube, a brass ring (sabot peeler ring) was glued facing the gun barrel. The flyer plate diameter was chosen to be 65 mm, which is slightly smaller than the inside diameter (66.5 mm) of the sabot peeler ring. We selected the entrance diameter D_I as 66 mm to have a clearance for the o-rings used in the piston to seal the pressure tube entrance. The pressure tube outside surface, at the front, was designed with a 30° inclination to allow the motion and expansion of the peeled sabot. Even though a

Fig. 6 Final design and dimensions of the water pressure tube (anvil)

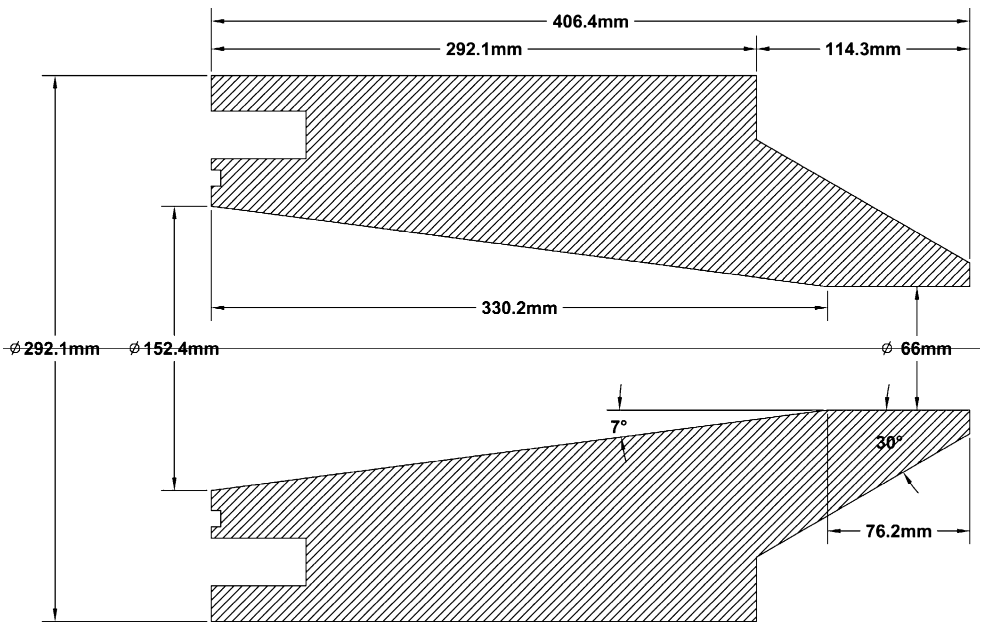

Fig. 7 A specimen panel (*left*) and a panel with a clamping ring (*right*)

certain amount of the projectile kinetic energy is dissipated by the sabot breaking, most of the projectile kinetic energy is transferred to the pressure tube. To avoid damage in the experimental setup, two shock absorbers (RCOS 2×6 BPM, Efdyn) were employed to dissipate the kinetic energy transferred to the pressure tube. The shock absorbers with a bore of 50.8 mm and a stroke of 152.4 mm have an energy absorption capacity of 19 kJ each. The shocks were connected to the pressure tube by a steel frame. Photographs of the newly developed FSI setup illustrating all the components are shown in Fig. 9. The pressure tube has two high pressure valves (HF9 60,000 psi, HiP high pressure equipment) one connected to an inlet pipe and the other to allow the exhaust of air while filling in with water. O-rings used at the front and back of the pressure tube were made of a 95 A Shore durometer fluorocarbon elastomer (V1238-95), which is suitable for underwater explosive loading. In the steel piston, double o-rings were used with two backup rings. The support of the pressure tube consisted of four ball bearings with adjustment capabilities to align the pressure tube to the gas gun barrel.

Experimental Procedures

The flyer plate and piston were ground and lapped to have parallel and flat impact surfaces. After assembly of the projectile, it was inserted into the gas gun barrel and placed at the end of the barrel (target chamber side). The specimen panel was coated with white paint to provide good contrast for the shadow moiré measurements. After painting, it was installed on the back of the anvil tube with an o-ring, a clamping ring and 12 screws. Shock absorbers and a fixture frame attached to the pressure tube were also assembled. The piston with two o-rings and two backup rings was inserted into the front of the pressure tube and aligned precisely perpendicular to the axis of the anvil tube. The anvil tube was filled up with water through a high-pressure valve, while air in the tube was exhausted through another valve. Alignment of the anvil tube against the flyer plate was made with great care to achieve planar impact between the flyer and piston. The target chamber and gas gun barrel were evacuated to a pressure below 100 Pa before the experiment to prevent the formation of an air cushion between the flyer plate and piston at impact. While evacuating the air, the piston with o-rings prevented the water from leaking. Nitrogen gas was pressurized into the breech up to 7 MPa, which, upon release, accelerated the projectile up to speeds of about 300 m/s. Upon impact, the impulsive pressure wave propagated through the fluid and pressure histories at various positions were measured by dynamic high-pressure transducers. Figure 10 shows the locations at which the transducers were

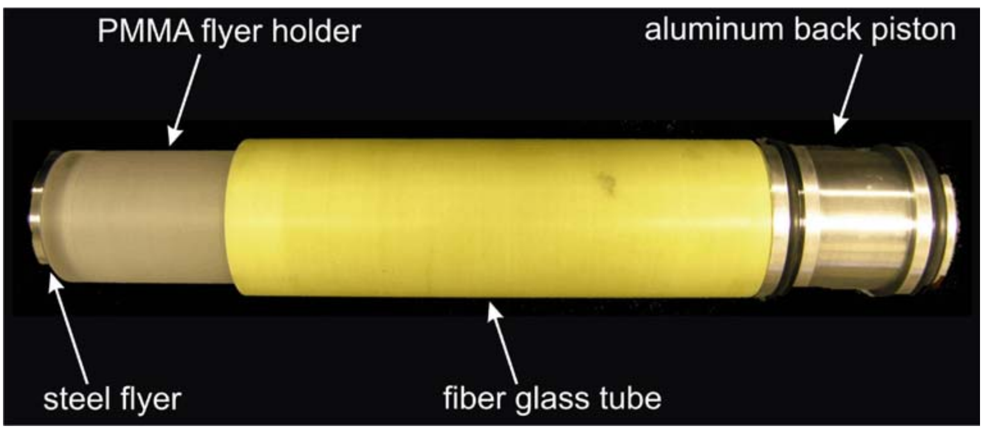

Fig. 8 Photograph of projectile assembly

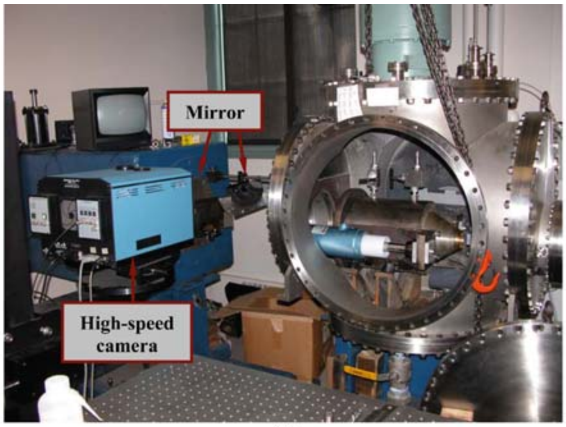

(a)

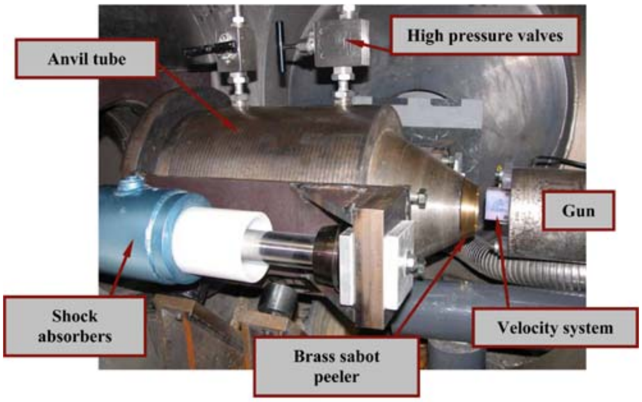

(b)

Fig. 9 Photographs of fluid–structure interaction experimental setup. (**a**) Outside of the target chamber and (**b**) inside of the target chamber

installed. A shadow moiré technique was used to measure the full field sample deformation history.

Diagnostics

Shadow Moiré

For recording the deformation of the plates in real time, during the impact, a combination of shadow moiré and high speed photography techniques have been used (see Fig. 11). The shadow moiré technique [1, 8] uses a linear grating of pitch size p to produce shadow fringes on the object; the same grid is used to view the object from a slightly different angle, hence, producing a moiré pattern. If the illumination and observation are done in perfectly collimated (parallel) light, it can be shown [1, 8] that the fringes are equal-depth fringes, the depth between two consecutive fringes being

$$w^{II} = \frac{p}{\tan\alpha_o - \tan\beta_o} \tag{13}$$

where α_o and β_o are the angles of illumination and of observation in collimated light, respectively. The upper index "II" is used to highlight the fact that this formula applies for collimated illumination and observation.

If the illumination and observation are done with non-parallel light, the angles α and β vary across the image field from $\alpha_0-\delta\alpha$ to $\alpha_0+\delta\alpha$ and $\beta_0-\delta\beta$ to $\beta_0+\delta\beta$, respectively. As a consequence, one can show that, in a

Fig. 10 Location of pressure sensors in the anvil and steel calibration plate

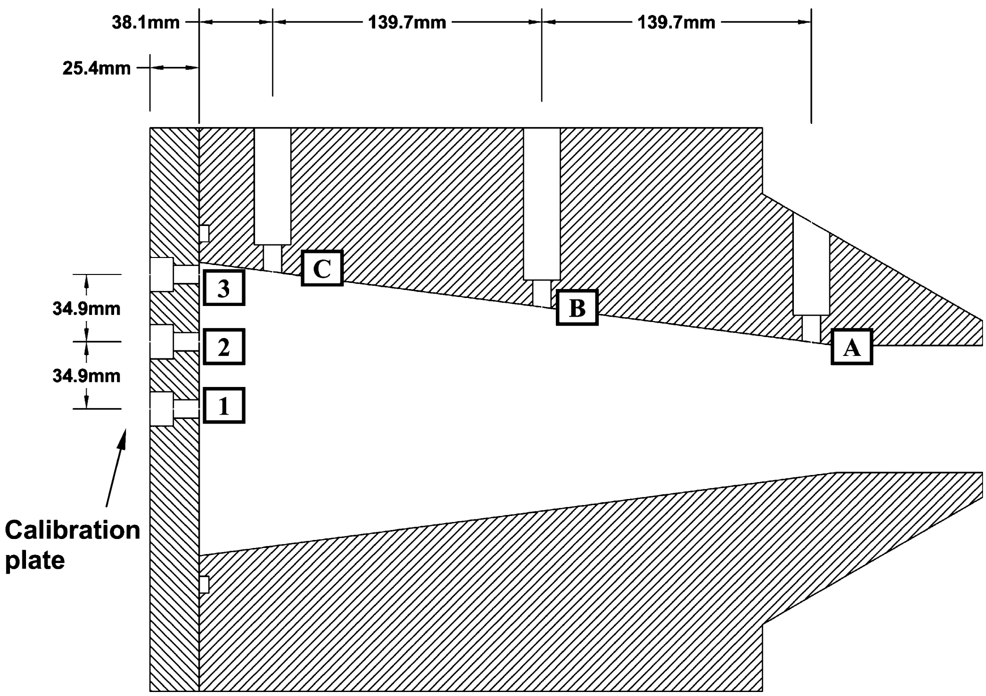

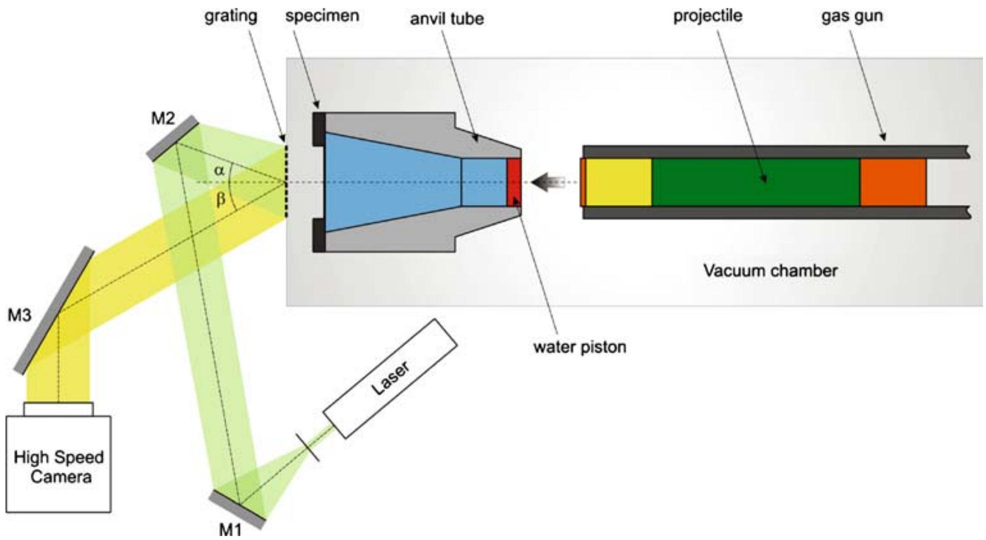

Fig. 11 Optical setup for recording shadow moiré fringes with a high speed camera

first order approximation, the fringe depth varies with the position in the image and equation (13) has to be corrected with a factor linear in the field cross-section coordinate x:

$$w = w^{II}\left[1 - x\frac{D_\alpha \cos\alpha_o - D_\beta \cos\beta_o}{D_\alpha D_\beta \sin(\alpha_o - \beta_o)}\right] = w^{II}[1 - \kappa x],$$
$$\text{with} \quad \kappa = \frac{D_\alpha \cos\alpha_o - D_\beta \cos\beta_o}{D_\alpha D_\beta \sin(\alpha_o - \beta_o)}, \tag{14}$$

where $D\alpha$ and $D\beta$ are the distances from the illumination point and observation point, respectively, to the center of the screen. Since these quantities are difficult to measure with sufficient accuracy, one determines the correction factor κ by fitting on images of objects with known profile (e.g., a sphere).

The shadow moiré setup was configured as shown in Fig. 11. A 5W solid-state diode-pumped, frequency-doubled Nd:Vanadate laser working at a wavelength of 532 nm was used as illumination source. A beam expander and two mirrors were used to direct the expanded light through the grating and onto the sample. The expanded spot size was 6.5” in diameter (same as the grating area), to cover the entire area of the sample. The observation was done through a third mirror with a high speed optical camera (Cordin Intensified CCD Camera 220-8, with 8-fold prism image divider) capable of recording frames with 8 CCD cameras at pre-programmable time intervals. The grating pitch was calculated such that the high speed camera could resolve spatially a maximum density of fringes supposed to be present in the experiment, which should typically correspond to a fringe depth of 2–3 mm on a spherical object of radius 5” (reproducing roughly the shape of the deformed plates, at maximum deformation). The grating was fabricated lithographically with a pitch of 508 mm (equal lines and spaces), on a 7×7” Cr mask plate used in the electronic industry. Since the focusing point of the camera was on the sample object, its surface was coated with a diffuse white paint, to eliminate direct reflection on the metal surface. The high speed camera was set close to maximum gain (255) and the frame-recording (shutter-opening) speed was typically 3 μs. The recording time had to be minimized for eliminating the motion blur, while still recording useful images on which to count the fringes. We accounted for <1/6 fringe change during the frame recording time (3 μs), which, according to our calculations and simulations, could be used for up to 300 m/s projectile velocities. The fringe count and data reduction was performed on images processed and enhanced using the Igor 4.0.8.0 (WaveMetrics Inc.) image processing kit.

The calibration of the image (pixels to mm) and the fringe depth and its variation across the image field were performed using several test objects. A radial optical target structure, with known lateral dimensions was used for the lateral calibration of the image (Fig. 12). The fringe depth across the image field was measured by taking images of a spherical object of known radius (R=125 mm) and doing a fit between a computer-generated shadow moiré grey level fringe pattern for a sphere in conditions of linear lateral fringe depth variation, and the recorded moiré pattern (Fig. 13). The fitting provided the value of the fringe depth at the center of the image (w) and the correction factor κ. Calibration images were taken before each experiment, to account for changes in the positions of the optics and sample alignment. Typical values were 0.42 mm/

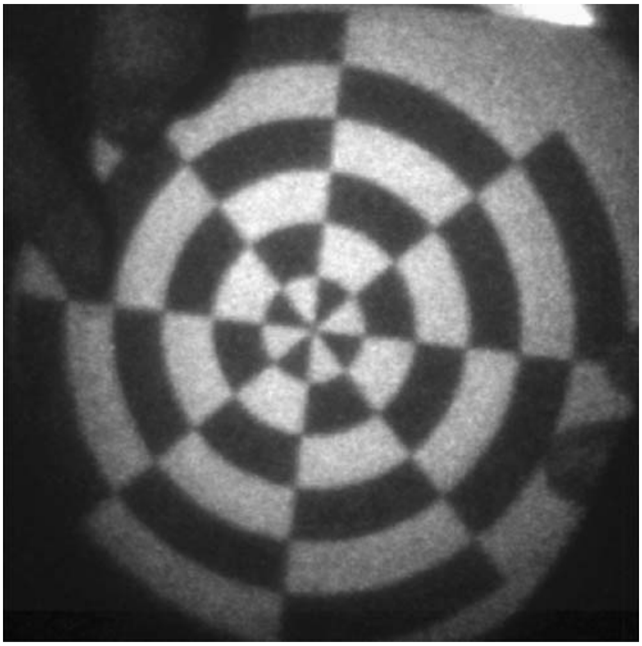

Fig. 12 Radial patterned used in shadow moiré calibration

pixel for the pixel-to-millimeter calibration in the image field, 2.7–3.7 mm/fringe for the fringe depth and 1.2–1.4×10^{-3} mm^{-1} for the correction factor κ.

Typical shadow moiré patterns recorded on the high speed camera will be presented in the next section reporting experimental results. Due to the fringe depth variation across the image and to the viewing angle effect, the moiré patterns loose their radial symmetry. This is related also to the necessity to have a non-symmetrical positioning of the incident and observation angles (α–β), to avoid direct reflections of the laser light into the camera objective from surfaces such as the vacuum chamber window and the grating itself. The retrieve of plate cross-sections from the moiré interferograms was performed using the image line profile function in the Igor image processing kit and by analyzing the image line profile with the multipeak fitting package (Gaussian peak profiles), to obtain the position of the maxima and minima of different interference orders. Due to the loss of contrast, image noise, higher fringe density, and viewing angle considerations at the edge of the sample plate, the fringe pattern in these regions could not be assessed with better than half-a-fringe accuracy. Since the overall height of the plate deformation is based on the fringe count starting from the edges, this error propagated to all fringes as a systematic error in estimating the absolute height of the deformation. However, the relative position of the fringes was of much higher accuracy (sub-pixel resolution due to the peak analysis procedure) and was not affected by this error, such that the shape of the retrieved deformation profiles is accurate. To get the absolute height of the deformation, an extrapolation of the profile curve at the edge was considered, such that the overall profile was risen or lowered until the deformation in the edge point of the sample was zero. For this operation, the edge closer to the incident illumination light was used (Fig. 11), where more fringes could be counted. An additional rotation of the profiles around the edge considered for this operation was performed, to account for the viewing angle effect, which was typically ~3–5° (same for all frames acquired during one experiment), accounting for the fine adjustment of the optics and small rotations of the camera around its axis.

Dynamic High Pressure Transducers

Measurement of pressure in the fluid is essential to assess the blast loading in the experimental setup. The pressure wave of a blast has very critical conditions such as a propagating velocity of about 1,500 m/s, a rise

Fig. 13 Shadow moiré fringe pattern corresponding to a spherical object of radius 125 mm recorded with the high speed camera in real conditions (*left*) and computer-generated moiré fringe pattern fitted to the real image (*right*)

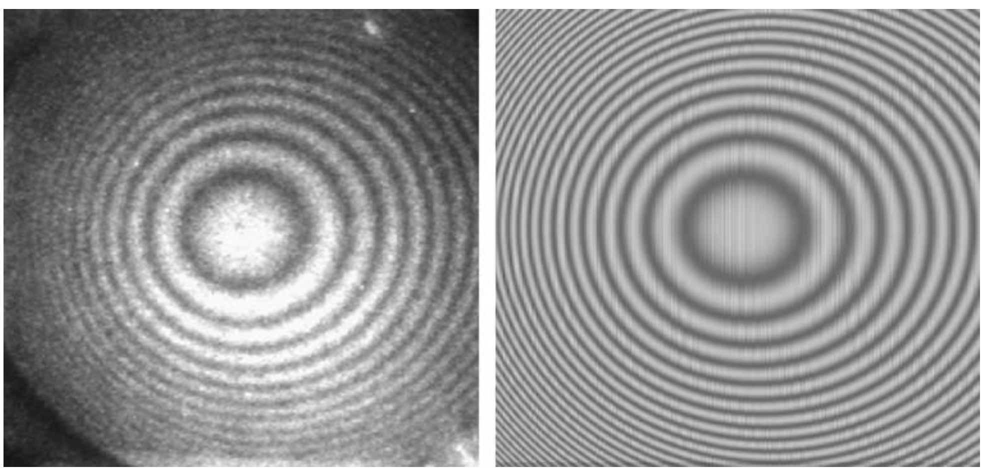

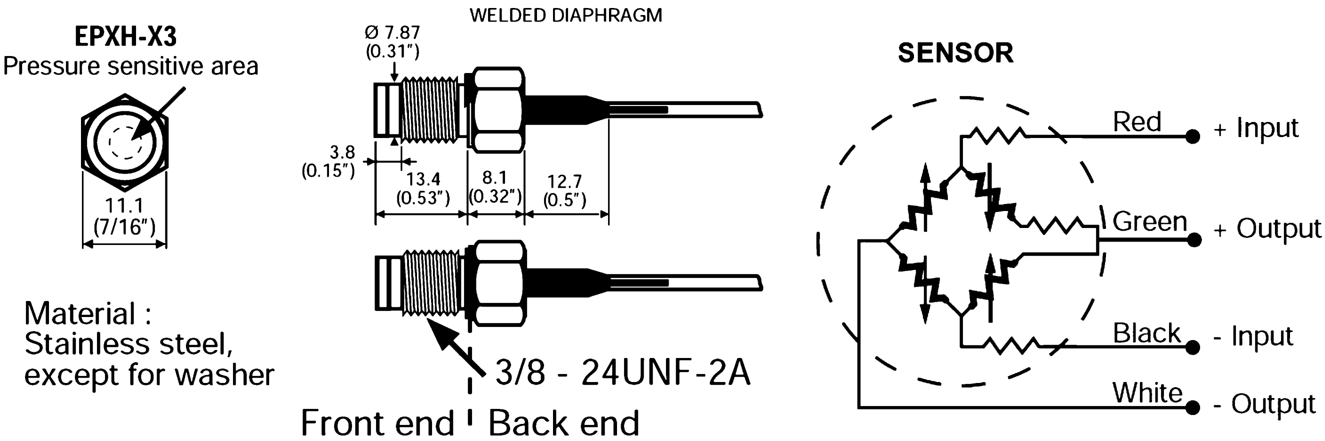

Fig. 14 Dynamic high-pressure transducers and circuit diagram (Wheatstone bridge) for the sensing resistors mounted on the diaphragm of the sensor

time shorter than 1 μs, a characteristic time scale about 10 μs, and pressure amplitude above 100 MPa. Due to its dynamic nature and the high pressure amplitude, special-purpose pressure transducers (EPXH-32, Entran) were employed in measuring the pressure in the fluid. The sensor is a diaphragm type transducer with four resistors installed on the diaphragm. The overall dimension of the sensor and the Wheatstone bridge configuration on the diaphragm are depicted in Fig. 14. The sensor was mounted with a copper o-ring by tightening up to 12 mN of torque. Parallel connection of direct current batteries of 9 V was used to excite the circuit. The circuit was implemented to minimize electromagnetic interference and avoid cross-talk between the sensors. All the connection wires were shielded and grounded, and the length of the wires was shortened as much as possible.

Experimental Results

Calibration

Experiment

Calibration experiments were performed to validate the functionality of the novel FSI experiment apparatus. Mounting a 25.4 mm-thick 4340 steel plate (Fig. 15) on the back of the pressure tube would provide an experimental assessment of the incident pressure wave in the absence of fluid–structure interaction (cavitation), which would result from deflection of a thin plate. In a calibration experiment, a projectile impact speed of 263 m/s was employed. A pressure sensor was mounted at position B (see Fig. 10) to avoid recording the superposition of the incident and reflective waves as it is the case of pressure measurements on the calibration plate. Figure 16(a) shows the recorded pressure history, which exhibited a steep rise, a peak pressure of about 118 MPa and subsequent exponential decay. The decaying time was in the order of 50 μs as expected. The reflection from the calibration plate is observed as a second peak at about 350 μs. In another calibration shot, the projectile was shot at 140 m/s. Pressure histories measured by transducers mounted on the calibration plate at positions 1 and 2 (see Fig. 10) are shown in Figs. 16(b) and (c). At these locations, the wave is the superposition of the incident and reflected waves. Hence, the pulse shape is much more convoluted than at location B. The peak pressure reached around 25–30 MPa which is much lower than the desired peak pressure of about 100 MPa. Obviously,

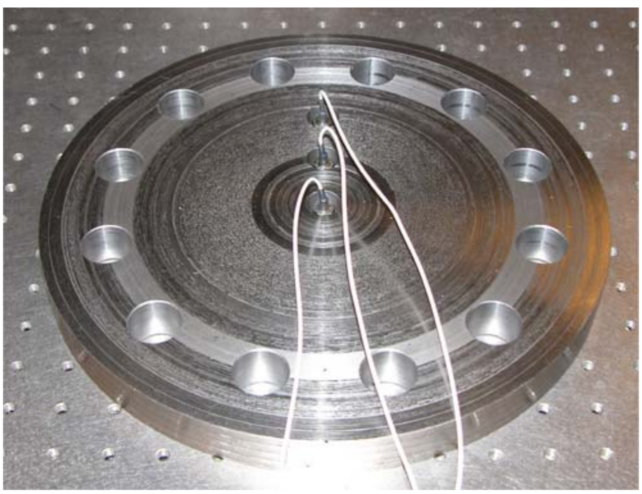

Fig. 15 Photograph of calibration plate with three pressure transducers installed

Fig. 16 Comparison of experimentally measured and FEM predicted pressure histories. (**a**) Pressure history at position B for a calibration shot with impact velocity of 263 m/s. (**b**) Pressure history at position 1 for a calibration shot with impact velocity of 140 m/s. (**c**) Pressure history at position 2 for a calibration shot with impact velocity of 140 m/s

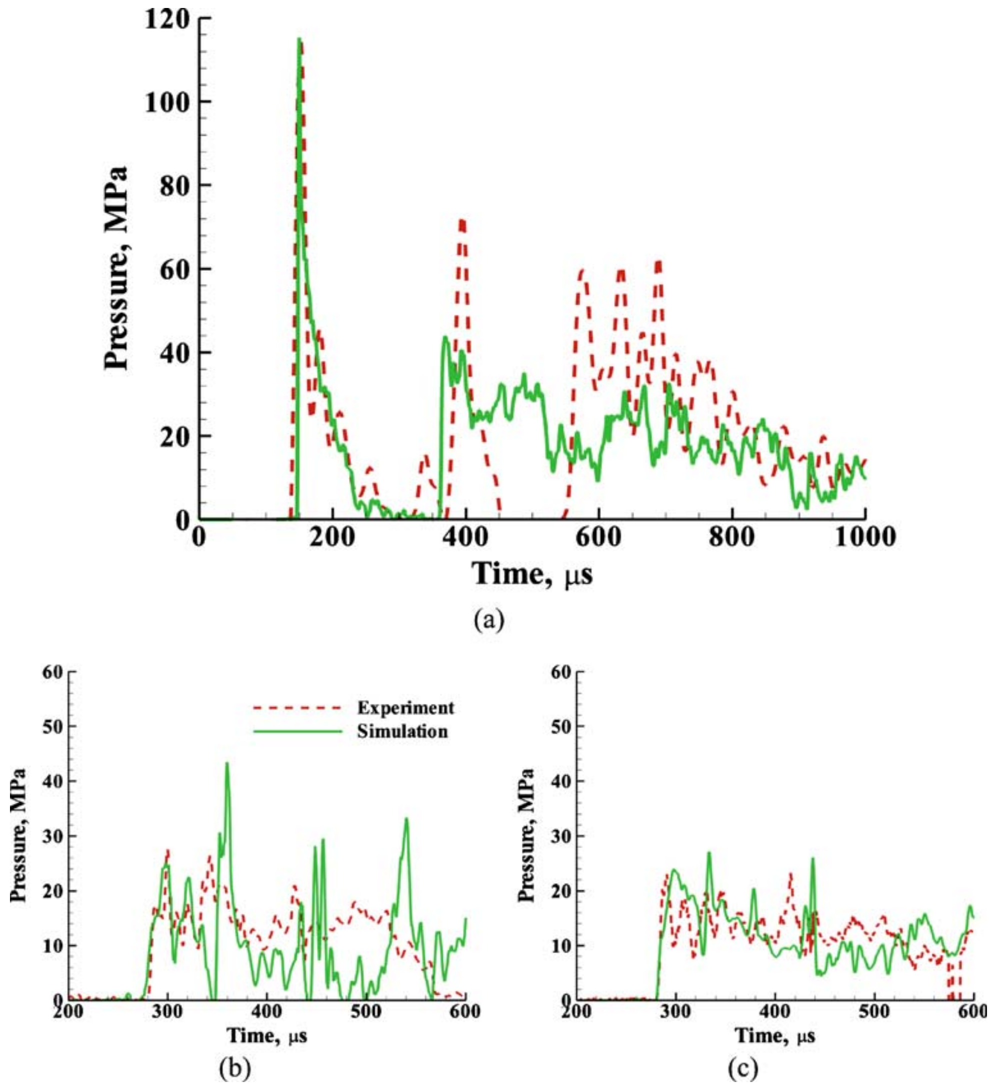

a projectile velocity of about 300 m/s is required to achieve a pressure level of 100 MPa.

Comparison with numerical modeling

To validate the calibration experimental results, Finite Element simulations were conducted using ABAQUS/explicit 6.4-1. Figure 17 shows the FE model of the calibration experiments in the FSI test setup. Due to the nature of the problem, two dimensional axi-symmetric 4-node elements with reduced integration were used. The total number of elements used in this simulation was 194,038. The material model for the anvil tube and calibration plate uses constitutive parameters for wrought 4340 steel while that of the piston and flyer plate uses constitutive parameters for heat-treated 4140 steel. The material properties used in the simulation are listed in Table 1. For water, a Mie–Grüneisen equation of state with a linear Hugoniot relation was used and a tensile pressure of 1 MPa was set to simulate water cavitation. Adaptive meshing was employed to prevent excessive element distortion in the water elements and a contact algorithm was employed to simulate impact between flyer, piston and water. The amplitudes and overall trends of the pressure histories predicted by the simulation are shown in Fig. 16. The plots show that the peak pressure, subsequent decay, and reflected pressure measured by the calibration experiment were well captured by the simulation during the time period of 280–600 μs. While measurement and simulation do not agree in every detail, silent features and peak pressures exhibit good agreement.

Figure 16(a) shows the exponential decay predicted by the numerical simulation. Very good agreement is observed between experimental record and simulated

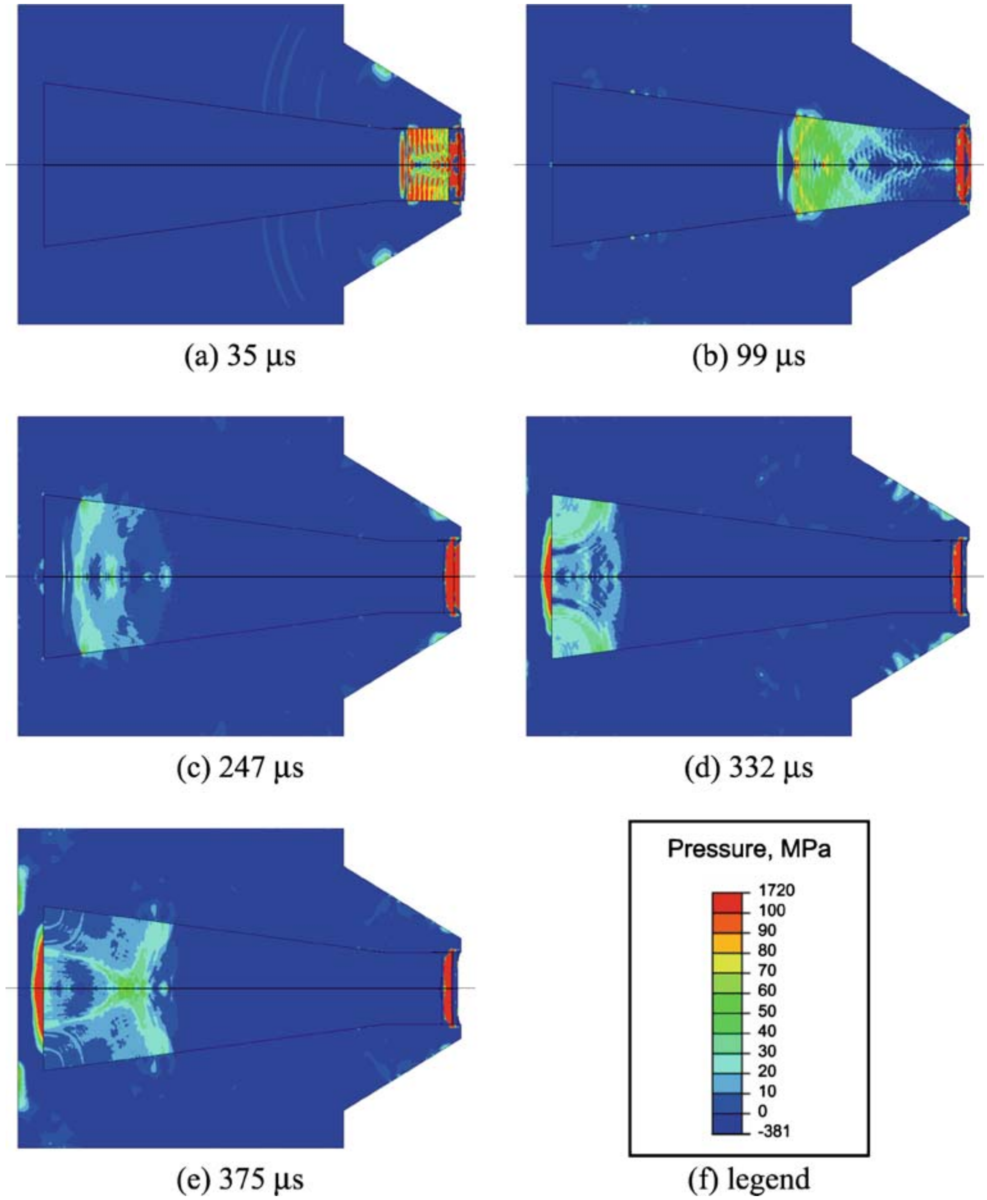

Fig. 17 Pressure contours obtained from axisymmetric finite element simulation. The sequence of images show the position of the pressure front at different times after the projectile impacted the water piston. The speed of the projectile in the simulation is 190 m/s

Table 1 Material properties used in the numerical analyses for heat-treated 4140 steel, wrought 4340 steel, and water

Material properties	Symbol	Units	Heat-treated 4140 steel	Wrought 4340 steel	Water
Young's modulus	E	GPa	205	205	–
Poisson's ratio	v	–	0.29	0.29	–
Density	ρ_0	kg/m^3	7,850	7,850	958
Yield stress	σ_0	MPa	1,000	470	–
Strain hardening $\sigma = K\varepsilon^n$					
hardening coefficient	K	MPa	1,615	470	–
hardening exponent	n	–	0.09	0	–
Equation of state $p = \frac{\rho_0 c_0^2 n}{(1-s_1 n)^2}\left(1-\frac{\Gamma_0 n}{2}\right)+\Gamma_0\rho_0 E_m, u_s = c_0 + s_1 u_p$					
Sound speed	c_0	m/s	–	–	1,490
EOS coefficient	s_1	–	–	–	1.92
Gruneisen coefficient	Γ_0	–	–	–	0.1

pressure history during this loading phase. The second pressure peak and its decay are also captured by the simulation although the agreement with the experimental measurement is less satisfactory. There are a number of factors that may contribute to that discrepancy, e.g., bubbles in the water, accuracy of the pressure gages, impact tilt, etc.

Figure 17 shows the evolution of the wavefront in time from the impact of the projectile against the water piston (assumed as $t = 0$ μs) up to 375 μs. After 35 μs [Fig. 17(a)] the front wave is still in the cylindrical conduct; when the front reaches the divergent diffuser [Figs. 17(b) and (c)] the pressure drops and the wavefront exhibits a small curvature. After about 300 μs the front reaches the monolithic plate and it is reflected. As it is shown in Fig. 17(d) there are two other reflected waves, one from each corner of the chamber. These two waves advance until they overlap, Fig. 17(e).

FSI test on a 304 Stainless Steel Monolithic Plate

Experiment

An annealed 304 stainless steel monolithic panel was tested to study the dynamic behavior of a solid plate subjected to underwater blast loading. The thickness of the plate was 1.84 mm. The measured impact velocity of the flyer plate was 314.85 m/s. Shadow moiré fringe patterns generated by the deformed specimen at 93, 193, 293, 393, 493, 643, 793, and 1,043 μs are shown in Fig. 18. The frame times correspond to times after the pressure front reached the plate surface in the water pressure tube. Figure 19 is a plot of the plate deflection history obtained by processing the shadow moiré fringe patterns following the data reduction procedure discussed in "Diagnostics." It is observed that the maximum deflection at the center of the specimen was achieved at about 393 μs and after that the plate merely oscillated with small amplitude due to elastic recovery. A pressure history at gage position C (see Fig. 10) was also measured. The normalized pressure history is shown in Fig. 20. We should mention that $p_0 = 82$ MPa was calculated by equation (13) and $t_0 = 25$ μs by equation (3). Note that time $t = 0$ corresponds to the time at which impact between flyer plate and piston occurs. The non-dimensional impulse applied to the plate was calculated based on p_0, t_0, and the material properties of the sample panel, i.e., $I/\left(M\sqrt{\sigma_y/\rho}\right) = 0.882$. The maximum deflection $\delta_{\max}$ was measured to be 29.83 mm and, thus, the non-dimensional maximum deflection is $(\delta/L)_{\max} = 0.391$. Figure 21 shows the deformation of the 304 stainless steel monolithic panel

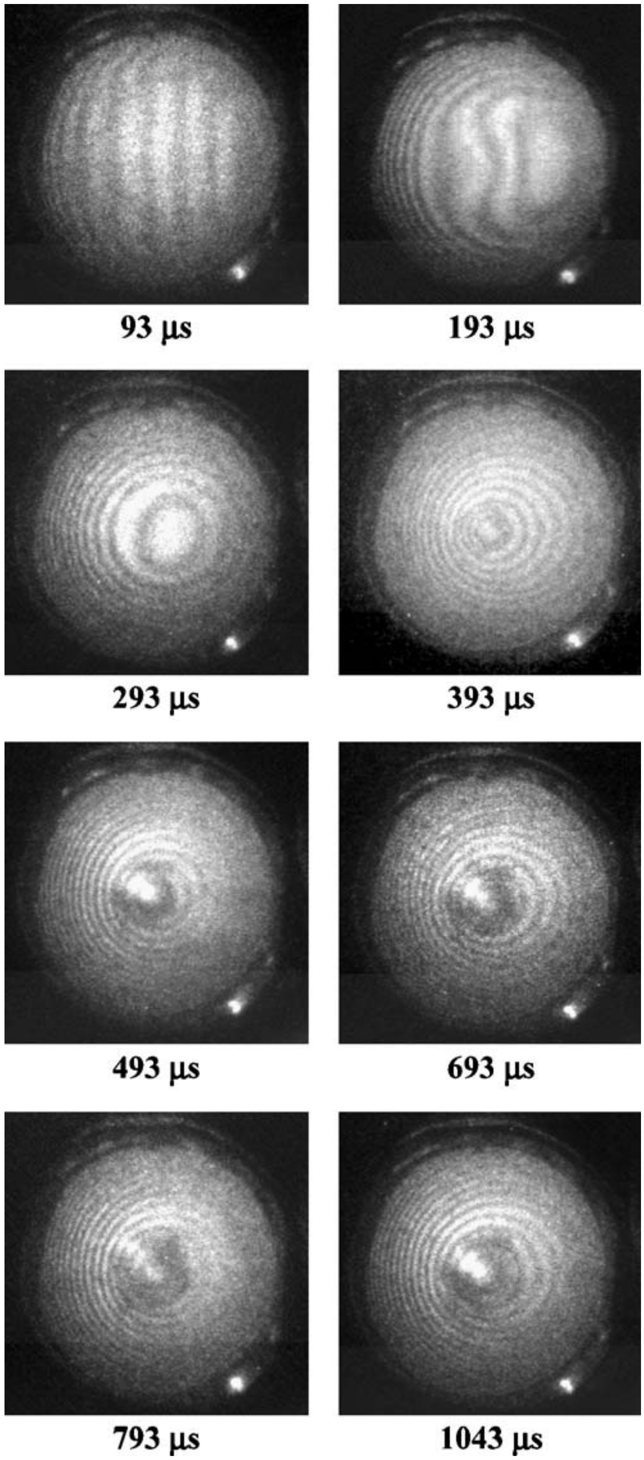

Fig. 18 Sequence of high-speed camera images showing shadow moiré fringes for the water blasted AISI 304 stainless steel monolithic specimen

obtained from postmortem digital photography. It should be noted that the white paint peeled off at certain regions of the plate in the clamping area. From this signature it is inferred that the plate slipped between the clamps. Additionally, one can observe the

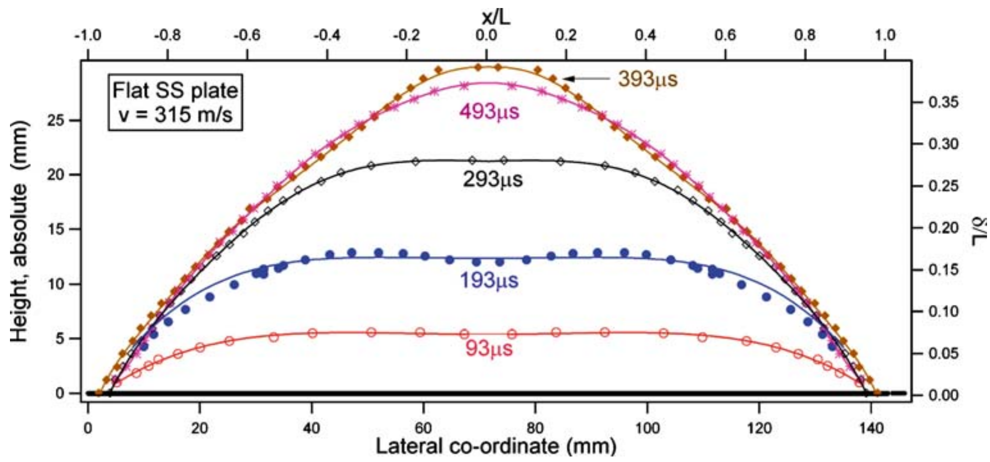

Fig. 19 Specimen out-of-plane configuration as measured by shadow moiré

ovalization of the screw holes in the radial direction of the specimen plate. Elongation of the clamped outside rim resulted in a radial boundary displacement of 1.0 mm all along the periphery of the specimen with diameter D. The slipping boundary condition resulted in a deflection larger than the deflection which would have occurred under perfectly fixed boundary conditions.

Comparison with numerical modeling

A numerical simulation of the above experiment was conducted to gain further insight into the fluid–structure interaction and assess the model predictive capabilities. The FE model was the same as that for the calibration case except that the calibration plate was replaced with a 1.84 mm thick 304 stainless steel solid plate. For the 304 stainless steel, the Johnson–Cook constitutive model was used, viz.,

$$\sigma_y = \left(A + B\left(\varepsilon_p^{eq}\right)^n\right)\left(1 + c\ln\dot{\varepsilon}^*\right)\left(1 - \left(T^*\right)^m\right) \quad (15)$$

$$where\ \dot{\varepsilon}^* = \frac{\dot{\varepsilon}_p^{eq}}{\dot{\varepsilon}_0}, T^* = \frac{T - T_{room}}{T_{melt} - T_{room}}.$$

ε_p^{eq} and $\dot{\varepsilon}_p^{eq}$ are equivalent plastic strain and equivalent plastic strain rate, respectively. T is the material temperature, T_{room} is the room temperature, and T_{melt} is the melting temperature of the material. The material properties and the Johnson–Cook parameters for the annealed 304 SS are given in Table 2. Figure 22 shows the predicted pressure history in relation to the

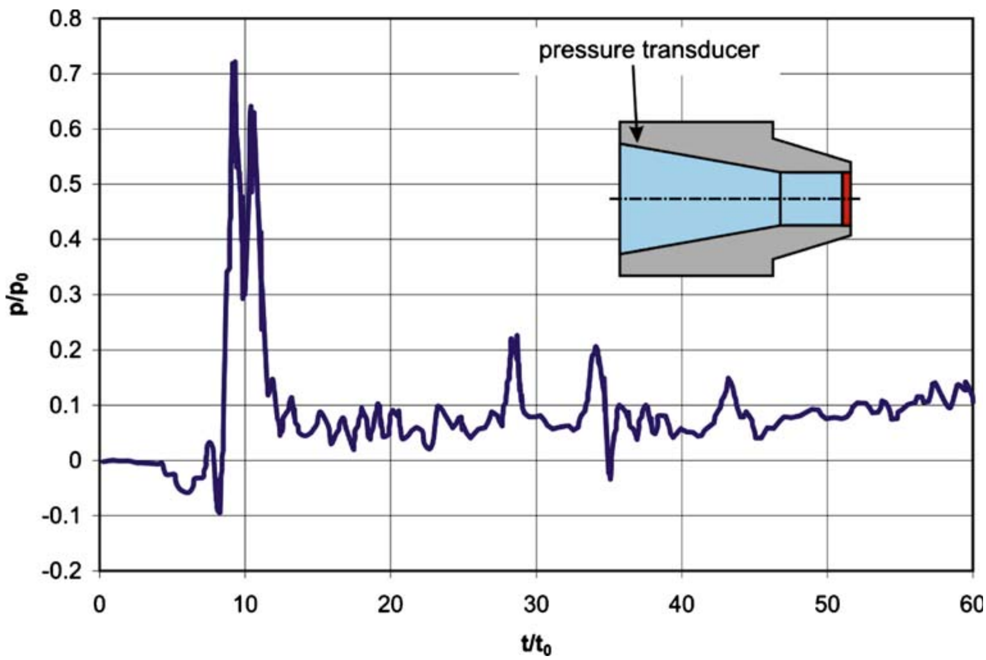

Fig. 20 Normalized pressure history measured by dynamic high pressure transducer placed at location C (p_0=82 MPa and t_0=25 μs)

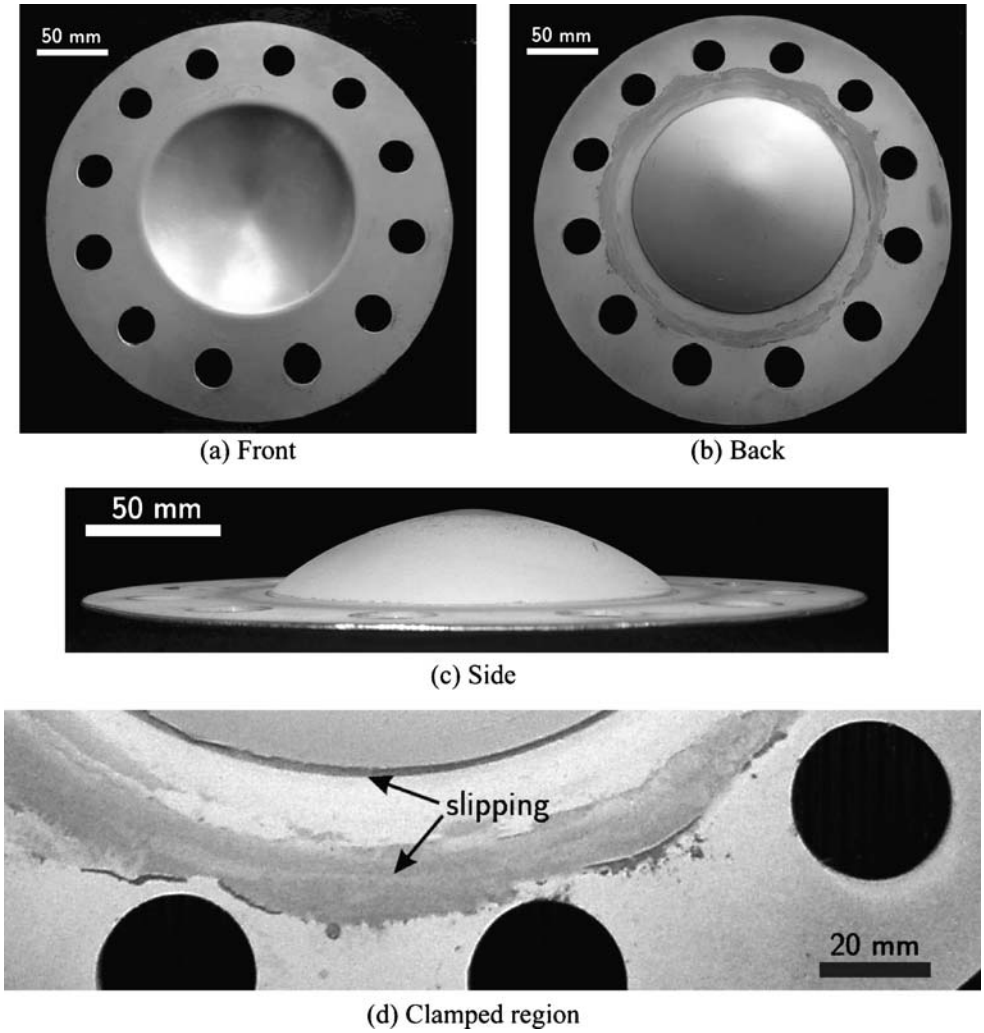

Fig. 21 AISI 304 stainless steel solid plate after blast loaded. (**a**), (**b**), and (**c**)show the front, the back and the side of the plate while (**d**) shows a region of the clam with clear evidence of slippage as highlighted with *arrows*. Note ovalization of the holes

experimentally measured one. The agreement is quite good taking into account that the pressure sensor was subjected to a sweeping pressure wave, which generates temporal pressure gradients, and as such oscillations of the sensor plate.

Figure 23 shows the pressure histories at different positions of the water tube from the FE simulation along a path near the axis of symmetry of the anvil tube. Due to the water tube geometry and material dissipation, the peak pressure decreases in time as the pressure wave propagates. At each position, exponential decay of the pressure history is observed, as expected.

In the simulation, perfectly clamped boundary conditions were considered so the deflection of the specimen plate was underestimated. Simulation of clamping, bolting and sliding is very complex. Therefore, in order to correct for the boundary flexibility, we considered the extra deflection induced by the sliding boundary condition as measured experimentally. The difference in the deflection between the case of perfectly clamped boundary and experimental result was assumed to be a linear function of the membrane reaction force history at the periphery of the plate, which is a function of time. Based on the measured

Table 2 Material properties and Johnson–Cook parameters for annealed 304 SS

Density (kg/m^3)	Young's modulus (GPa)	Poisson's ratio	Melting temperature (K)	Room temperature (K)	Specific heat (J/kg K)
7,900	200	0.3	1,673	293	440
A (MPa)	B (MPa)	n	c	$\dot{\varepsilon}_0(\mathrm{s}^{-1})$	
310	1,000	0.65	0.07	1.00	1.00

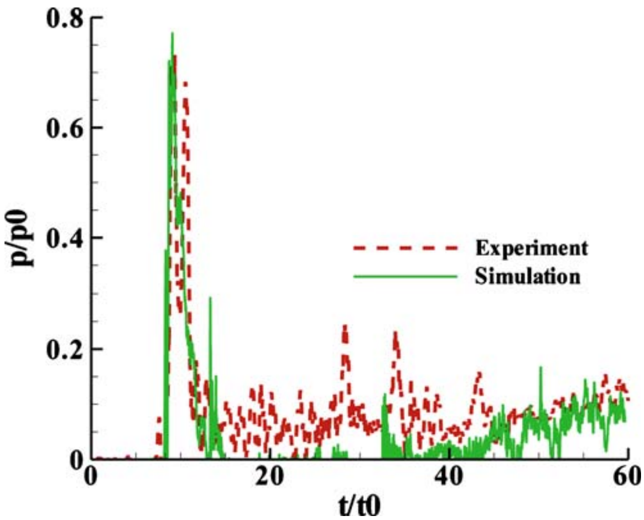

Fig. 22 Pressure histories as measured by dynamic high pressure transducer and predicted by FEM simulation (p_0=81.7 MPa and t_0=25.4 μs)

maximum boundary sliding of about 1 mm (see Fig. 21), the extra deflection was then computed and added to the numerical prediction for the time at which the specimen deflection reaches its maximum (393 μs) and then it was scaled in time with the numerically computed reaction force history [Fig. 24(b)]. The reaction force as a function of time presents some noise due to the numerical temporal and spatial interpolation used in the FEM simulation. Hence, it was smoothed with a Savitzky–Golay on a moving window of 7,000 points and a polynomial of the first degree [15]. The resultant deflection obtained by the simulation accounting for the extra deflection due to sliding is shown in Fig. 24(a). Comparison with the deflection history measured by shadow moiré, also shown in Fig. 24(a), reveals a very good agreement.

Figure 25 shows the development of cavitation as predicted by the FEM simulation. The time in which the projectile impacts the water piston is taken as reference, i.e., $t=0$ [see Fig. 25(a)]. After 280 μs the pressure wave reaches the specimen that starts to deform [see Fig. 25(b)]. At this instant, there is a small volume of cavitation near the specimen. This volume is not on the axis of symmetry because the deforming plate presents an off center maximum velocity in the early deformation phase [see deformation shape at 93 μs in Fig. 25(a) and Fig. 25(c)]. Note that this feature leads to the existence of two maxima in the plate deflection, as revealed by the experimental measurements [see

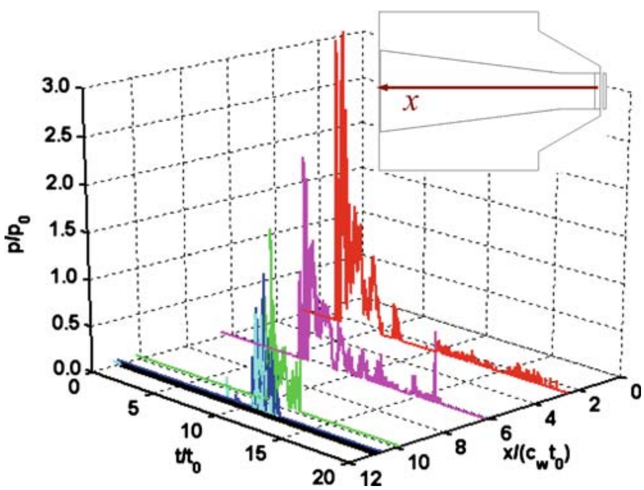

Fig. 23 Simulated pressure histories, at different positions along path 2 (near the axis of the tube), for the monolithic plate subjected to a water blast

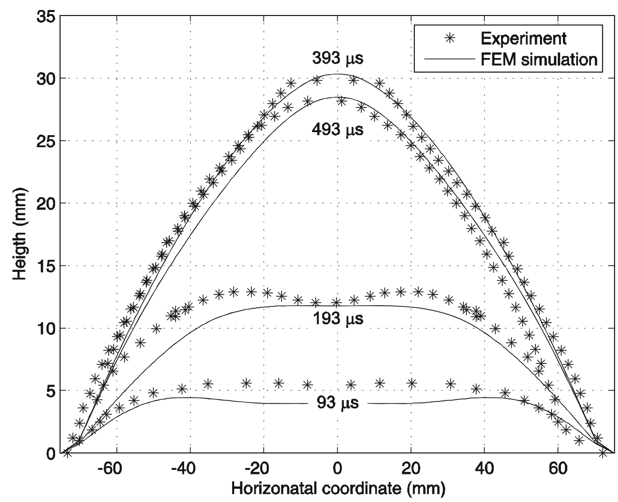

(a)

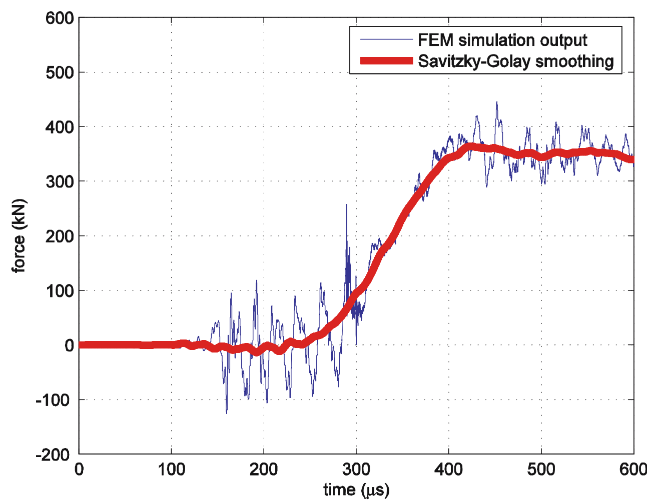

(b)

Fig. 24 (**a**) Comparison between experimentally measured and simulated specimen deflections at different time instances. (**b**) Membrane reaction force history used to scale the additional specimen deflection due to boundary slippage

Fig. 24(a)]. In fact the two maxima is a little more pronounced in the experimental signatures than in the numerical simulations. What is more important, such behavior is the result of the non-uniform pressure history resulting from the fluid-structure interaction. After 514 μs the cavitation zone grows and moves towards the axis of symmetry [see Fig. 25(d)]. After 535 μs the cavitation volume starts to shrink and at 556 μs it is completely filled with water [see Fig. 25(e)]; in the meanwhile the plate is still deflecting and the water cavitates on the periphery near the anvil tube [see Fig. 25(e)]. At 620 μs the plate exhibits a conical shape with a rounded tip [see Fig. 25(f)]. Cavitation in the center is observed at 1,002 μs [see Fig. 25(g)] until it reaches its maximum expansion at 1,172 μs [see Fig. 25(h)]. After this the cavitation volume shrinks and at 1,512 μs it is completely filled with water [see Fig. 25(i)].

To understand the cavitation phenomenon, it is useful to analyze the pressure and velocity histories in the water. Figure 26 shows the pressure distribution along a path between the axis of symmetry and the periphery (see figure inset) at different time instances in the FE simulation. As shown before in Fig. 23, the peak pressure decreases in time as the pressure wave propagates along the anvil. The reflection of the pressure wave is observed at the dimensionless time $t/t_0 = 12.7$. Between the front face of the plate and the reflection wavefront, cavitation occurs at the place

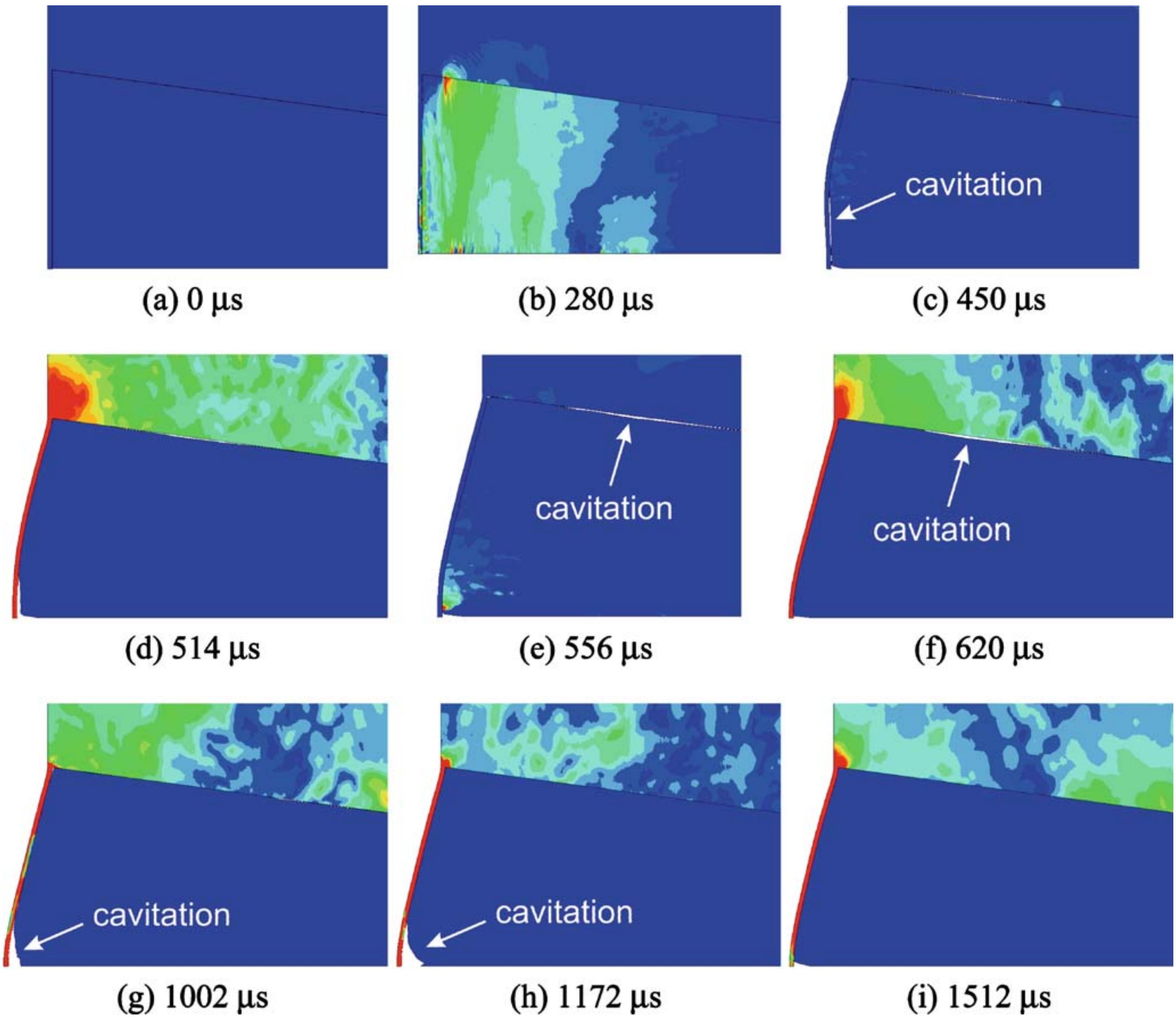

Fig. 25 Contours of pressure history for water blasted AISI 304 stainless steel solid plate. The simulation reveals the cavitation history as the specimen deforms. Time t=0 corresponds to the time at which the flyer plate impacts the piston. The *arrows* highlight locations where cavitation takes place

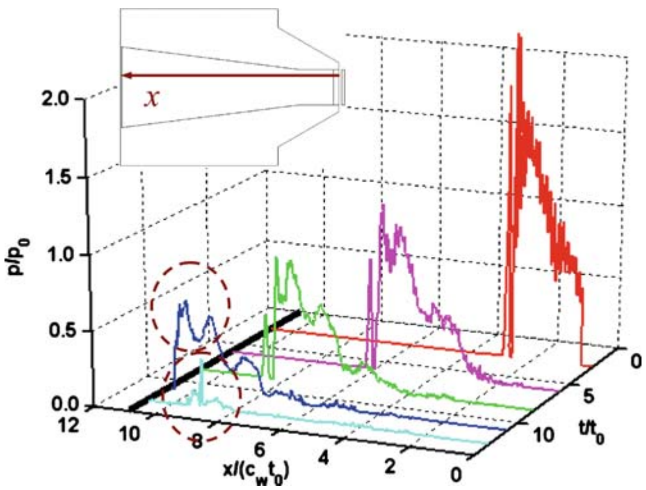

Fig. 26 Simulated pressure distributions along the path shown in the inset at various normalized times. The *circles* highlight pressure wave reflection and cavitated (zero pressure) region

where water pressure becomes lower than −1 MPa (tension). The velocity distributions at different instances in the FE simulation are shown in Fig. 27. At the dimensionless time $t/t_0 = 12.7$, the water adjacent to the plate moves with the plate in the positive x-direction, while neighbor water has a negative velocity, which implies it moves backward. This is a clear indication that the pressure between these two zones is negative (tension) which leads to cavitation.

Concluding Remarks

A novel experimental methodology which incorporates fluid–structure interaction was proposed to be able to assess the dynamic deformation of *structures* subjected to underwater blast loading. The concept of the experimental setup is to employ the impact of a specially designed projectile against a fluid, e.g., water to generate an impulsive loading similar to the loading produced in an underwater blast. In order to design a laboratory scale experiment, a non-dimensional analysis was conducted to scale down full field applications, e.g., naval structures. Finite Element analyses were performed to determine the validity and potential of the FSI setup. In particular, a diffuser type pressure tube was designed and validated with the aid of FE simulations. The design was implemented in a gas gun together with several diagnostic tools including projective velocity, measured by pin-type velocity sensors, pressure history, measured by dynamic membrane-type pressure transducers, and specimen panel out-of-plane full field displacements, measured by means of shadow moiré and high-speed photography.

Calibration experiments were performed that confirmed the capability of the new FSI setup to generate exponentially decaying pressure histories resembling blast loading conditions. Simulation of the wave propagation event showed that the known EOS for water can reproduce the measured pressure histories accurately. To investigate the FSI effect, we tested a 304 stainless steel monolithic plate. The dynamic deformation behavior of the plate and pressure history was successfully measured by shadow moiré and a pressure sensor, respectively. The numerical simulations were found in good agreement with these measurements and provided additional understanding on the specimen deformation history, plastic strains and *cavitation phenomenon*.

It is important to realize that scaling large structures subjected to dynamic loading to laboratory dimensions is a very complex problem. In fact scaling both spatial and temporal variables (length, strain rates, etc.) is a very difficult problem. For a discussion of this feature see the book by Norman Jones [7]. In this context, changing the material to scale both dimensions and deformation rates may be worth pursuing. In this case the challenge is to change all relevant material properties, density, modulus, strength, failure strain, heat capacity, etc. such that the failure modes are also the same. In the context of energy dissipation, it is worth mentioning that boundary conditions are particularly relevant to scaling. Our goal was to develop an experimental technique that could mimic full field applications as much as possible with the purpose of exploring fsstructural and material issues *through performance comparison*. Numerical simulation could then be used to assess the effect of scaling. In this

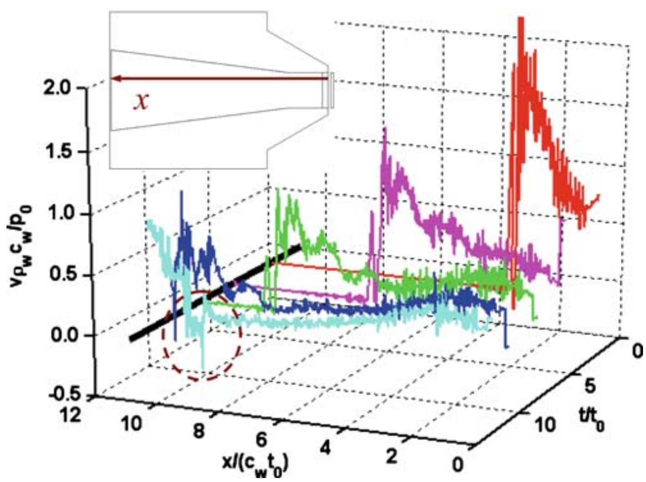

Fig. 27 Simulated velocity distributions in the x-direction along the path shown in the inset at various normalized times. The circle highlights the change of the sign of water velocity which corresponds to cavitation

regard, model accuracy can be demonstrated by capturing all relevant features observed in the FSI lab and other lab setups.

The developed FSI technique has the potential to assess the efficacy of many structural concepts, including sandwich panels made of various materials and core topologies, when subjected to impulsive loading. Also it can be used to compare various metal alloys, especially design for blast applications, exhibiting very high strength without significant loss of ductility. The technique not only offers the possibility of interrogating materials and structures in the plastic regime but also identify fracture initiation and propagation. We have demonstrated this feature for the case of steel sandwich panels with honeycomb and pyramidal cores. The findings will be reported in a subsequent publication.

Acknowledgments This work was sponsored by the Office of Naval Research under Award No. 123163-02-N00014-02-1-0700. The authors are deeply grateful to John Hutchinson from Harvard University for pointing out important scaling issues and helpful discussions. We would also like express our gratitude to Lapo Mori for his assistance in the preparation of the manuscript and its critical review. A special thank is due to Huang Tang and Francois Barthelat for assistance with the numerical simulations and experiments.

References

1. Cloud GL (1995) Optical methods of engineering analysis. Cambridge University Press, Cambridge, New York.
2. Deshpande VS, Fleck NA (2005) One-dimensional response of sandwich plates to underwater shock loading. J Mech Phys Solids 53(11):2347–2383.
3. Espinosa HD, Nemat-Nasser S (2000) Low-velocity impact testing. ASM Handbook 8:539–559.
4. Fleck NA, Deshpande VS (2004) The resistance of clamped sandwich beams to shock loading. J Appl Mech—Trans Am Soc Mech Eng 71(3):386–401.
5. Hao S, Liu WK, Moran B, Vernerey F, Olson GB (2004) Multi-scale constitutive model and computational framework for the design of ultra-high strength, high toughness steels. Comput Methods Appl Mech Eng 193(17–20):1865–1908.
6. Hutchinson JW, Xue ZY (2005) Metal sandwich plates optimized for pressure impulses. Int J Mech Sci 47(4–5):545–569.
7. Jones N (1997) Structural impact. Cambridge University Press, Cambridge, UK.
8. Kobayashi AS (1993) Handbook on experimental mechanics, 2nd ed. SEM, New York, NY, pp 287–296.
9. Liang Y, Spuskanyuk AV, Flores SE, Hayhurst DR, Hutchinson JW, McMeeking RM, Evans, AG (2006) The response of metallic sandwich panels to water blast. J Appl Mech (in press).
10. Qiu X, Deshpande VS, Fleck NA (2004) Dynamic response of a clamped circular sandwich plate subject to shock loading. J Appl Mech—Trans Am Soc Mech Eng 71(5):637–645.
11. Qiu X, Deshpande VS, Fleck NA (2003) Finite element analysis of the dynamic response of clamped sandwich beams subject to shock loading. Eur J Mech A Solids 22(6):801–814.
12. Qiu X, Deshpande VS, Fleck NA (2005) Impulsive loading of clamped monolithic and sandwich beams over a central patch. J Mech Phys Solids 53(5):1015–1046.
13. Rabczuk T, Kim JY, Samaniego E, Belytschko T (2004) Homogenization of sandwich structures. Int J Numer Methods Eng 61(7):1009–1027.
14. Radford DD, Deshpande VS, Fleck NA (2005) The use of metal foam projectiles to simulate shock loading on a structure. Int J Impact Eng 31(9):1152–1171.
15. Savitzky A, Golay MJE (1964) Smoothing and differentiation of data by simplified least squares procedures. Anal Chem 36 (8):1627–1639.
16. Smith PD, Hetherington JG (1994) Blast and ballistic loading of structures. Butterworth–Heinemann, Oxford, UK.
17. Swisdak MM (1978) Explosion effects and properties—Part II: explosion effects in water, technical report, Naval Surface Weapons Center, Dahlgren, Virginia.
18. Taylor GI (1963) The pressure and impulse of submarine explosion waves on plates. In: Batchelor GK (ed) The scientific papers of Sir Geoffrey Ingram Taylor, Volume III: Aerodynamics and the mechanics of projectiles and explosions. Cambridge University Press, Cambridge, UK, pp 287–303.
19. Vaynman S, Fine ME, Asfahani RI, Bormet DM, Hahin C (2002) High performance copper-precipitation-hardned steel. In: Proceedings from Materials Solutions Conference 2002, 7–9 October, Columbus, Ohio, ASM International, pp 43–48.
20. Vaynman S, Fine ME, Bhat SP (2004) High-strength, low-carbon, copper-precipitation-strengthening steels for tank car application. In: Materials Science and Technology 2004 Conference Proceedings, pp 417–421.
21. Xue ZY, Hutchinson JW (2004) A comparative study of impulse-resistant metal sandwich plates. Int J Impact Eng 30(10):1283–1305.
22. Xue ZY, Hutchinson JW (2003) Preliminary assessment of sandwich plates subject to blast loads. Int J Mech Sci 45(4):687–705.